RSC Advances

PAPER

View Article Online
View Journal | View Issue

Check for updates

Cite this: *RSC Adv.*, 2023, **13**, 36477

Mixed valence copper oxide composites derived from metal–organic frameworks for efficient visible light fuel denitrification†

Jian Li,[a] Renkun Huang, *[abc] Lu Chen, [bc] Yuzhou Xia, [bc] Guiyang Yan [bc] and Ruwen Liang *[bc]

Received 4th November 2023
Accepted 8th December 2023

DOI: 10.1039/d3ra07532j

rsc.li/rsc-advances

The construction of heterojunctions has been used to optimize photocatalyst fuel denitrification. In this work, HKUST-1(Cu) was used as a sacrificial template to synthesize a composite material Cu_xO (CuO/Cu_2O) that retains the original MOF framework for photocatalytic fuel denitrification by calcination at different temperatures. By adjusting the temperature, the content of CuO/Cu_2O can be changed to control the performance and structure of Cu_xO-*T* effectively. The results show that Cu_xO-300 has the best photocatalytic performance, and its denitrification rate reaches 81% after 4 hours of visible light (≥420 nm) irradiation. Through the experimental analysis of pyridine's infrared and XPS spectra, we found that calcination produces Cu_xO-*T* mixed-valence metal oxide, which can create more exposed Lewis acid sites in the HKUST-1(Cu) framework. This leads to improved pyridine adsorption capabilities. The mixed-valence metal oxide forms a type II semiconductor heterojunction, which accelerates carrier separation and promotes photocatalytic activity for pyridine denitrification.

Introduction

Fossil fuels are the most critical and valuable energy source in the world. Human development and environmental change are closely related to their use.[1,2] A large number of nitrogen-containing compounds (NCCs), such as pyridine and pyrrole, are produced in the use of fuels (gasoline and diesel).[3–5] Combustion will lead to NO_x emissions, pollute the environment, and seriously affect human health through the respiratory tract.[6] Therefore, research on removing NCCs from crude gasoline fuel has become a global hotspot.[7,8] Currently, the classical technology used in industry to remove nitrogen species from fuels is hydrodenitrogenation (HDN). However, this method requires high temperature and pressure conditions, which increase the cost.[9] This has shifted people's attention towards photocatalytic one-pot removal of NCCs, a more environmentally friendly technology.[10] The search for better gasoline fuel denitrification photocatalysts is a top priority in fuel purification research.

Currently, researchers aim to use Bi-based or Co-based materials for photocatalytic removal of NCCs.[11–14] However, these materials still have low catalytic efficiency and unstable chemical properties. Several studies indicate that adding Cu enhances the material's pyridine adsorption and promotes photocatalytic reaction. Lu *et al.* introduced Cu to enhance the photocatalytic denitrification ability of a CuCo-ZIF bimetallic material.[15] Pure copper oxide (CuO) and cuprous oxide (Cu_2O) are promising catalysts due to their p-type semiconductor properties and narrow band gap (1.2 eV and 2 eV, respectively).[16] However, the high recombination rate of photogenerated carriers and low photocatalytic activity of copper oxide limit its practical application.[17,18] At the same time, the performance of a catalyst is affected by its morphology.[19] Porous nanostructures with high specific surface area and excellent photogenerated carrier transport properties are considered to be critical components of photocatalytic materials.[20–22]

Metal–organic frameworks (MOFs) exhibit high specific surface area and ease of synthesis.[23–25] The metal–organic framework can serve as a template for synthesizing porous metal oxides through self-sacrifice.[26,27] The MOF derivatives prepared in this way not only improve the thermal/chemical stability of the original parent MOF but also retain the original fascinating structural characteristics of the parent MOF, such as large surface area, tunable structure, and surface permeability, which better enhance the photocatalytic performance of the material.[28–30] Moreover, compared with traditional metal oxides, the porous structure of MOF-derived metal oxides has a larger number of active sites, which enhances their

[a]*State Key Laboratory of Photocatalysis on Energy and Environment, Fuzhou University, Fuzhou 350002, China*

[b]*Province University Key Laboratory of Green Energy and Environment Catalysis, Ningde Normal University, Ningde 352100, China*

[c]*Fujian Provincial Key Laboratory of Featured Materials in Biochemical Industry, Ningde Normal University, Ningde 352100, China. E-mail: t1432@ndnu.edu.cn; Tel: +86-15860671891*

† Electronic supplementary information (ESI) available. See DOI: https://doi.org/10.1039/d3ra07532j

Open Access Article. Published on 14 December 2023. Downloaded on 1/19/2026 11:32:41 PM. This article is licensed under a Creative Commons Attribution-NonCommercial 3.0 Unported Licence.

Open Access Article. Published on 14 December 2023. Downloaded on 1/19/2026 11:32:41 PM.
This article is licensed under a Creative Commons Attribution-NonCommercial 3.0 Unported Licence.

adsorption and catalytic ability.[31–33] Cu-based MOFs were used as templates to synthesize CuO/Cu_2O with the original framework. Bagheri *et al.* discovered that by transforming Cu-based MOFs into CuO, they could efficiently promote the conversion of 4-nitrophenol to 4-aminophenol while retaining some of the crystal structure of HKUST-1 (Quasi-MOF).[34] The construction of heterojunctions can accelerate the electron transfer of materials and improve the catalytic performance.[35,36] Currently, most studies on producing metal oxide nanoparticles through Cu-MOF pyrolysis focus on their application in gas adsorption and organic conversion.[37,38] However, there are limited reports on using CuO/Cu_2O nanoparticles, which retain the original octahedral MOF framework, for photocatalytic fuel denitrification.

In this paper, copper-based MOF (HKUST-1) with high adsorption was selected as the ideal pre-sacrifice for the preparation of mixed valence metal oxide Cu_xO (CuO/Cu_2O), and the photocatalytic denitrification performance of Cu_xO generated under different temperature gradients was investigated. The results showed that Cu_xO-*T* with HKUST-1(Cu) octahedral framework showed more vital visible light activity for denitrification of typical NCCs (such as pyridine), and Cu_xO-300 exhibited the best degradation rate of 81% for pyridine. Finally, the possible photocatalytic reaction mechanism and the action form of active sites were discussed. This work demonstrates the excellent performance of Cu-based catalysts for removing NCCs. It confirms the feasibility of improving photocatalytic activity by calcination retaining the original MOF structure to expose its active sites and form mixed-valence metal oxides.

Experimental

Reagents and chemicals

1,3,5-Benzene tricarboxylic acid (H_3BTC, 98%) was supplied by Aladdin Reagent Co., Ltd (Shanghai, China). Copper(II) nitrate trihydrate ($Cu(NO_3)_2 \cdot 3H_2O$, 99 wt%), sodium hydroxide (NaOH, 97 wt%), *N*,*N*-dimethylformamide (DMF, 99.5 wt%), anhydrous ethanol (EtOH, 99.5 wt%), pyridine (99.5 wt%), and octane (99.5 wt%) were purchased by Sinopharm Chemical Reagent Co., Ltd (Shanghai, China). All chemical reagents are of analytical grade and used as received.

Preparation of HKUST-1 (Cu)

HKUST-1(Cu) catalyst was prepared by solvothermal method. Firstly, 2.00 g Cu $(NO_3)_2 \cdot 3H_2O$ (8.29 mmol) and 1.00 g 1,3,5-benzene tricarboxylic acid (4.76 mmol) were weighed and dissolved in 24 mL 1 : 1 : 1 (volume ratio) deionized water/DMF/EtOH mixed solvent, respectively. Then the above solution was mixed and continued to stir until a uniform blue mixed solution was obtained. The above-mixed solution was transferred to a 100 mL hydrothermal reactor with polytetrafluoroethylene lining and reacted at 85 °C for 20 h. After the reaction, it was naturally cooled to room temperature and filtered. Finally, the product was washed several times with ethanol and then placed in a vacuum drying oven at 60 °C for 24 h to obtain the catalyst HKUST-1(Cu).

Preparation of mixed-valence Cu_xO

HKUST-1(Cu) was used as a pre-sacrificial body, and a suitable sample was weighed and placed in a ceramic crucible and a muffle furnace. Firstly, the temperature was heated to 300 °C at a heating rate of 5 °C min^{-1}, and then the temperature was increased to 350 °C, 400 °C, and 500 °C at a rate of 2 °C min^{-1}. When the specified temperature was reached, the sample was kept in a muffle furnace for two hours (Fig. S1†). Then it was taken out after cooling to room temperature to obtain black powder Cu_xO-*T* (Cu_xO-300, Cu_xO-350, Cu_xO-400, Cu_xO-500 according to the calcination temperature *T*). In addition, flake CuO nanomaterials were prepared by hydrothermal method for comparison.

Characterization

X-ray diffraction (XRD) patterns were obtained using a Bruker D8 Advance X-ray powder diffractometer. Fourier transform infrared reflectance (FT-IR) spectra were measured using a Shimadzu infrared spectrophotometer. TESCAN MIRA4 field emission scanning electron microscope (SEM) and Tecnai G2 F20 S-TWIN (FEI) transmission electron microscope (TEM) were used to analyze the morphology of the prepared samples. The pieces ' X-ray photoelectron spectroscopy (XPS) profiles were obtained using a Thermo Fisher K-Alpha instrument equipped with a monochromatic Al Lα X-ray source. UV-Vis diffuse reflectance spectroscopy (DRS) of the samples was performed using a Shimadzu UV-2700 UV-Vis-IR spectrophotometer in the 250–800 nm wavelength range. Photocurrent measurement using BAS Epsilon workstation. Electrochemical impedance spectroscopy (EIS) experiments using a precision PARC workstation.

Photocatalytic activity measurements

First, 70 mg of pyridine was dissolved in 1.0 L of *n*-octane to prepare 100 μg g^{-1} of simulated gasoline fuel containing NCCs. Then, 50 mg of photocatalyst and 50 mL of pyridine/*n*-octane solution (100 μg g^{-1}) were added to the quartz reactor. The suspension was stirred in the dark for two hours to ensure adsorption–desorption equilibrium. After that, the suspension was irradiated with a 300 W xenon lamp (PLS-SXE 300) equipped with an ultraviolet cut-off filter to cut off light with a less than 420 nm wavelength. During the selected time interval, the equipartition of the suspension was removed and centrifuged. The Varian Cary 60 spectrometer was used to monitor the remaining pyridine concentration in the supernatant. The maximum absorbance measured at different reaction times was converted to the denitrification ratio of pyridine. The expression is denitrification ratio of pyridine $= (C_0 - C_t)/C_0 \times 100\%$.

Results and discussion

Characterization of the prepared samples

The XRD spectra of HKUST-1(Cu) and Cu_xO-*T* composites are shown in Fig. 1. The position of each diffraction peak in HKUST-1(Cu) agrees with the situation reported in the literature.[39,40] With the increase in calcination temperature, the XRD peak

© 2023 The Author(s). Published by the Royal Society of Chemistry

Open Access Article. Published on 14 December 2023. Downloaded on 1/19/2026 11:32:41 PM.
This article is licensed under a Creative Commons Attribution-NonCommercial 3.0 Unported Licence.

intensity of HKUST-1(Cu) gradually decreased, indicating that the skeleton collapsed. At a temperature of 250 °C, both HKUST-1(Cu) and Cu_xO still exhibit XRD diffraction peaks. At 300 °C, only CuO (PDF # 80-1917) and Cu_2O (PDF # 65-3288) diffraction peaks are visible, while those of HKUST-1(Cu) disappear. At 300 °C, 350 °C, and 400 °C, the XRD local amplification spectrum of Cu_xO-*T* composites reveals the presence of the characteristic Cu_2O peak at 36.5°.[41] However, at 500 °C, the Cu_2O peak disappears entirely, which suggests that Cu_2O undergoes a conversion to CuO at high temperatures (Fig. 1(b)). Thermogravimetric analysis was conducted on HKUST-1(Cu) in Fig. 1(c). The compound decomposes gradually with increasing temperature, causing the initial loss of free/bound water molecules. Tricarboxylic acid deteriorated significantly at 300 °C, leading to substantial weight loss. At last, the TGA curve leveled off around 350 °C. To protect the MOF template structure and remove organic ligands, HKUST-1(Cu) was converted to Cu_xO at 300 °C. Choose a temperature between 350-600 °C for the second step to convert Cu_xO into CuO and determine the maximum temperature that destroys the MOF structure.

Fig. S2(a)† shows the typical FT-IR spectra of HKUST-1(Cu) and Cu_xO-*T* composites. The peaks at 1645 and 1445 cm^{-1}, indicated –O–C–O– bond. Meanwhile, the absorption peak at 1368 cm^{-1} is associated with the stretching mode of C–O. The bending vibration peak of the C–H bond at 940 cm^{-1}. The bands locate at 721 and 488 cm^{-1} may be related to the bending mode and stretching mode of Cu–O, respectively. The band at around 721 cm^{-1} confirms the coordination of Cu^{2+} and –COOH.[42] With the increase in calcination temperature, the disappearance of characteristic peaks from each functional group confirmed ligand decomposition of HKUST-1(Cu). This is in agreement with the XRD results, confirming successful pyrolysis and sample preparation.

The samples' surface area and pore structure were measured by N_2 desorption–adsorption. With the rise in calcination temperature, the BET-specific surface area and pore volume of Cu_xO-*T* samples decreased significantly due to the decomposition of organic ligands in the framework (Fig. S2(b) and Table S1†). The BET-specific surface area of Cu_xO-300 is about 17.68 $m^2\ g^{-1}$, and the pore volume is about 0.154 $cm^3\ g^{-1}$. Compared to Cu_xO at other temperatures, Cu_xO-300 has a larger specific surface area. This means that more active sites can be provided to improve catalytic performance.

The SEM images of HKUST-1(Cu) and Cu_xO-*T* composites are shown in Fig. 2. The crystal size of HKUST-1(Cu) is 5–7 μm, with a typical octahedral structure and a very smooth surface (Fig. 2(a)).[43] Fig. 2(b) and (c) shows the sheet-like nanostructures of CuO as a control. As shown in Fig. 2(d), the morphology of the sample (Cu_xO-250) obtained at the lowest calcination temperature is similar to that of HKUST-1(Cu). Still, the surface begins to be gradually decorated by Cu_xO particles, and the morphology becomes unsmooth, attributed to the pyrolysis of MOF in the air. As the calcination temperature increases (Cu_xO-300) (Fig. 2(e) and (f)), Cu_xO particles gradually form, creating a rough surface with a thick dot shape while still maintaining an octahedral structure. Fig. 2(g) and (h) shows that increasing the calcination temperature leads to higher crystallization rates, larger particle sizes, and uniform distribution in Cu_xO-350 and Cu_xO-400 samples. However, when the temperature rises to 500 °C, the morphology and structure of Cu_xO-500 (Fig. 2(i)) are destroyed, Cu_xO is pyrolyzed, the particles fall off, and direct rapid heating is not conducive to maintaining the porous structure of MOF.

Additionally, energy dispersive spectroscopy (EDS) spectrum was used to explore the elemental composition of the material. Random regions of Cu_xO-250, Cu_xO-300 and Cu_xO-500 are selected for detection, respectively (Fig. S3(a)–(c)†). Obtain Cu_xO-250, Cu_xO-300 and Cu_xO-500 corresponding EDS spectrum (Fig. S3(d)–(f)†). From the EDS spectrum of Cu_xO-250 several well-defined peaks were evident related to C, Cu and O, but in Cu_xO-300 and Cu_xO-500, the carbon content is drastically reduced. Trace carbon to maintain the original framework. Changes in the ratio of Cu to O at different temperatures are also indirectly evidenced by changes in Cu^+/Cu^{2+} content.

TEM images of as-prepared HKUST-1 sample reveal regular octahedron morphology having smooth surface (Fig. S4†). The TEM images in Fig. 3(a) show the octahedral shape of Cu_xO-300 particles, preserved even after pyrolysis, with scattered edges visible. In Fig. 3(b), high-resolution TEM images of Cu_xO-300 are presented. The images show lattice fringes with a spacing of 0.30 nm and 0.25 nm, corresponding to the (110) lattice plane of Cu_2O and the (002) lattice plane of CuO, respectively.[44,45] It has been confirmed that the synthesis of Cu_xO-300 was successful.

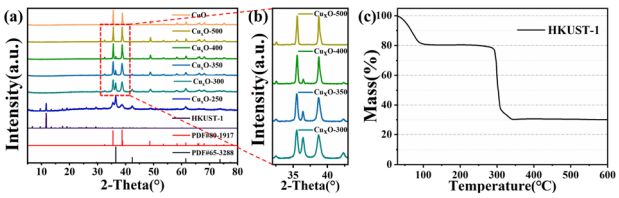

Fig. 1 (a) X-ray diffraction pattern; (b) enlarged XRD patterns in the 2θ range from 32 to 42°; (c) Thermogravimetric analysis curve of HKUST-1 in air atmosphere.

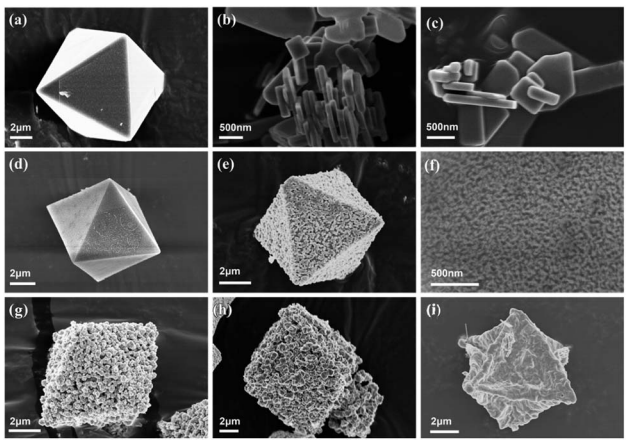

Fig. 2 (a) SEM images of HKUST-1(Cu), (b and c) flake CuO, (d) Cu_xO-250, (e and f) Cu_xO-300, (g) Cu_xO-350, (h) Cu_xO-400 and (i) Cu_xO-500.

Open Access Article. Published on 14 December 2023. Downloaded on 1/19/2026 11:32:41 PM.
This article is licensed under a Creative Commons Attribution-NonCommercial 3.0 Unported Licence.

The elemental composition and valence state of Cu_xO-*T* were determined by XPS, and the oxidation state of Cu element on the surface of Cu_xO-*T* composites was studied by high-resolution XPS (Fig. 4). The spectrum mainly shows the proportion of different valence Cu elements at different temperatures Cu_xO, and semi-quantitative analysis is carried out. The two characteristic peaks at 952.5 and 932.8 eV correspond to the binding energies of Cu^+ $2p_{1/2}$ and $2p_{3/2}$ electrons, while the two characteristic peaks at 953.8 and 933.8 eV correspond to the binding energies of Cu^{2+} $2p_{1/2}$ and $2p_{3/2}$, respectively.[46,47] In addition, satellite peaks with $2p_{1/2}$ and $2p_{3/2}$ peaks were also observed, corresponding to the electronic oscillation,[48] indicating the presence of Cu^{2+} and the coexistence of Cu_2O and CuO on Cu_xO-*T*. It can be found that in Cu_xO-*T*, the ratio of Cu^+/Cu^{2+} gradually decreases with the increase in temperature, and the ratio of Cu_xO-300 is the highest at other temperatures, while Cu_xO-500 is the lowest.

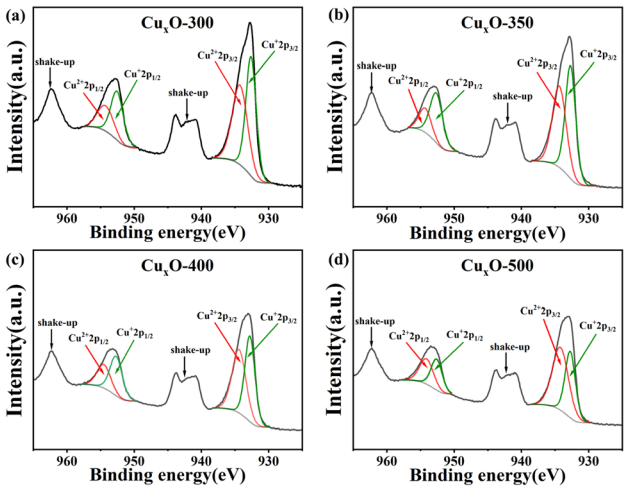

Fig. 4 (a) Cu_xO-300, (b) Cu_xO-350, (c) Cu_xO-400, and (d) Cu_xO-500 Cu 2p high-resolution XPS spectra.

Photocatalytic performance

The photoactivity of Cu_xO-*T* for NCCs (such as pyridine) denitrification was evaluated by visible light ($\lambda \geq 420$ nm). As shown in Fig. 5, the dark reaction indicates that pyridine denitrification almost does not occur under dark conditions. Under light irradiation, Cu_xO-300 exhibited higher photocatalytic activity within 240 min compared with flaky CuO (~15%). Fig. 5(a) corresponds to pyridine denitrification efficiency between Cu_xO-*T* and CuO. Among the four samples prepared by the two-step calcination method, the Cu_xO-300 sample has the highest photocatalytic activity (~81%). The kinetic data of the pyridine denitrification reaction are shown in Fig. 5(b). The rate constants of Cu_xO-300, Cu_xO-350, Cu_xO-400, Cu_xO-500, and flaky CuO were calculated to be 0.345, 0.235, 0.015, 0.010, and 0.025 h^{-1}, respectively. The quantitative analysis data show that the photocatalytic activity of Cu_xO-300 is about 12.8 times higher than that of flaky CuO synthesized by the hydrothermal method. The high photoactivity of Cu_xO-300 can be attributed to (i) Cu_xO-300 has a relatively high specific surface area based on maintaining the original MOF structure, which is conducive to the adsorption of pyridine molecules on the surface of Cu_xO;[49] (ii) the formation of tiny Cu_xO particles in this unique octahedral structure exposes more active sites of unsaturated valence metal centers, and the distance between the carrier and the surface active site is shorter; (iii) Cu_xO small particles have superior optical properties, and the transport distance between carriers is shorter, which is conducive to the separation of carriers. However, too high a temperature to generate larger Cu_xO particles destroys the MOF structure, causes more CuO to cover the active sites of Cu_2O, increases the particle spacing, and hinders the carrier's reaction with pyridine molecules. In summary, the Cu_xO-300 composite material is beneficial in improving its photocatalytic denitrification ability for pyridine (Table S2†).

In order to determine the active sites of the materials, we performed acidity tests on the pyridine-FTIR spectra of the better-performing samples. As shown in Fig. 6, the pyridine-FTIR spectra of Cu_xO-300 and Cu_xO-350 showed a sharp peak at 1441 cm^{-1}, indicating the presence of Lewis acid center, and a sharp peak at 1530 cm^{-1} indicating the presence of Brønsted acid center.[11] The mixture of acids in Cu_xO-300 and Cu_xO-350 was dominated by Lewis acid. Furthermore, pyridine can readily bind to the central metal Lewis acid in Cu_xO-300 and Cu_xO-350 due to its Lewis base properties. The exposed Cu^+/Cu^{2+} metal active center can be a Lewis acid to absorb the basic pyridine through coordination. This suggests that Cu_xO-*T* exhibits a high affinity towards pyridine. In addition, Cu_xO-300 has a significantly higher concentration of Lewis and Brønsted acid sites than Cu_xO-350

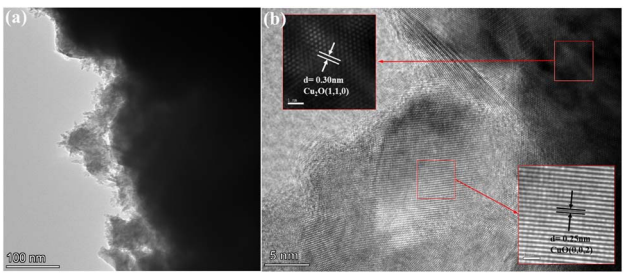

Fig. 3 (a) Transmission electron microscope (TEM) of Cu_xO-300 and (b) high-resolution TEM of Cu_xO-300.

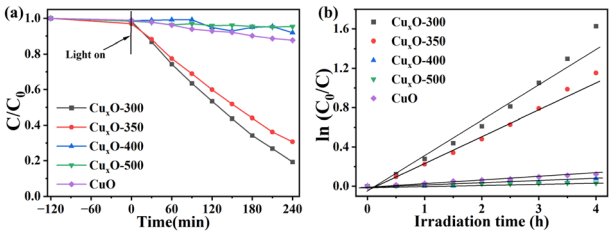

Fig. 5 (a) Photocatalytic denitrification of pyridine under different conditions; (b) pyridine denitrification kinetics in the presence of CuO, Cu_xO-300, Cu_xO-350, Cu_xO-400, Cu_xO-500. Reaction conditions: 50 mg catalyst in 50 mL 100 μg g^{-1} pyridine/octane solution.

© 2023 The Author(s). Published by the Royal Society of Chemistry

Open Access Article. Published on 14 December 2023. Downloaded on 1/19/2026 11:32:41 PM.
This article is licensed under a Creative Commons Attribution-NonCommercial 3.0 Unported Licence.

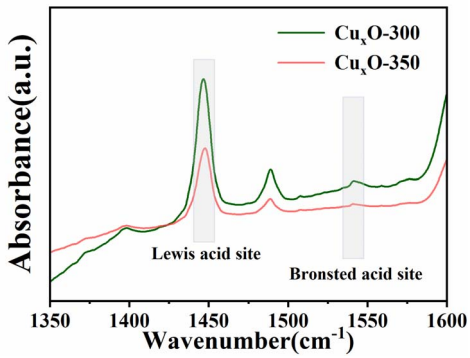

Fig. 6 Py-FTIR of Cu$_x$O-300 and Cu$_x$O-350.

approximately 2.02 times more. As a result, Cu$_x$O-300 is more effective in adsorbing pyridine, thanks to its excellent content of metal-centered acid sites. This enhances the transfer and separation of photogenerated carriers. The superior photocatalysis of Cu$_x$O-300 is due to this reason.

The reusability and stability of the Cu$_x$O-*T* photocatalyst were studied. As shown in Fig. S3(a) and (b),† the photocatalytic activity of Cu$_x$O-300 is still high after four reaction cycles, indicating good catalytic stability. The crystal structure of the photocatalyst used remained unchanged compared to the fresh photocatalyst, as seen from the XRD analysis.

Photocatalytic mechanism

Photoelectrochemical experiments were carried out further to explain carrier transfer and separation efficiency. Fig. 7(a) displays the transient photocurrent response curve, which reveals that Cu$_x$O-300 exhibits the highest photocurrent intensity when exposed to light. This indicates that Cu$_x$O-300 has a longer lifetime of photogenerated electron–hole pairs than other synthesized materials, resulting in more effective separation and transfer of photogenerated carriers.[42] To better understand the excellent carrier transport properties of Cu$_x$O-300, we drew the EIS Nyquist diagram (Fig. 7(b)), whose arc radius reflects the solid interface delamination and surface charge transfer resistance.[50] The radius of Cu$_x$O-300 is the smallest, indicating that Cu$_x$O-300 can minimize the interface charge transfer resistance and increase the carrier charge transfer ratio. In summary, Cu$_x$O-300 with more mixed valence unsaturated active sites can reduce the recombination rate of photogenerated carriers and accelerate separation and transfer.

Synthesised materials were studied for absorption spectra by employing UV-Visible Diffuse reflectance spectra that is illustrated in Fig. S6.† However, the overall black color of the synthetic material makes it difficult to determine its optical properties by DRS. XPS valence band (VB-XPS) was able to identify the valence band (VB) maximum of CuO and Cu$_2$O (Fig. S7(a) and (b)†). According to the VB-XPS plots of Cu$_x$O, the VB maximum of CuO and Cu$_2$O was calculated to be 2.05 eV and 1.46 eV. The contact potential difference between the sample and the XPS analyzer was used to compute the VB potential of the normal hydrogen electrode ($E_{\text{VB-NHE}}$, *vs.* NHE, pH = 6.8) using the following calculation: $E_{\text{VB-NHE}} = \phi + E_{\text{VB-XPS}} - 4.44$, where ϕ was the electron work function (4.55 eV) of the XPS analyzer, and $E_{\text{VB-XPS}}$ was the VB measured from the VB-XPS plots.[14] Therefore, the $E_{\text{VB-NHE}}$ value of CuO and Cu$_2$O was calculated to be 2.16 and 1.57 eV. As shown in Fig. S7(c) and (d),† Mott–Schottky plots were used to estimate the flat band potential (E_{fb}).[51] The E_{fb} value is determined from the corresponding intercepts of the linear plot region with the potential axis of Cu$_2$O and CuO being 1.37 and 1.95 eV *vs.* Ag/AgCl at pH = 6.8, equivalent to 1.57 and 2.16 eV *vs.* the normal hydrogen electrode (NHE) at pH = 6.8. Furthermore, the Mott–Schottky plots of Cu$_2$O and CuO exhibited negative slopes, indicating that Cu$_2$O and CuO is an p-type semiconductor.

The most reliable and direct method is ESR to study the photocatalytic mechanism of Cu$_x$O-300 composite fuel denitrification. ESR analysis used DMPO as a trapping agent to determine the formation of $^{\bullet}$OH radicals and $^{\bullet}O_2^-$ radicals in solution under visible light irradiation. As shown in Fig. 8(a), in the presence of Cu$_x$O-300, the 6-line signal can be observed under illumination. As the illumination time increases, the DMPO-$^{\bullet}O_2^-$ gradually increases, indicating that $^{\bullet}O_2^-$ is the primary active substance in the reaction process. However, after 10 min of illumination, the signal of DMPO-$^{\bullet}$OH was still relatively weak, which meant that $^{\bullet}$OH was not the primary active substance of the reaction (Fig. 8(c)). This is because the valence band (VB) maximum of Cu$_2$O (1.57 eV *vs.* NHE) and CuO (2.16 eV *vs.* NHE) is lower than that of $E_{(H_2O/OH)}$ (2.27 eV *vs.* NHE),[52,53] while the conduction band (CB) minimum of Cu$_2$O (−0.63 eV *vs.* NHE) is higher than that of $E_{(O_2/^{\bullet}O_2^-)}$ (−0.33 eV *vs.* NHE).[33] Therefore, the generation of $^{\bullet}$OH radicals may be more likely due to the combination of $^{\bullet}O_2^-$ and H^+ to form $^{\bullet}$OH. The TEMPO molecule can be considered a hole probe because hole oxidation can gradually quench its free radicals. As shown in Fig. 8(b), the ESR signal of TEMPO is weakened, confirming the generation of photogenerated holes. The above measurement results show that Cu$_x$O-300 can provide abundant

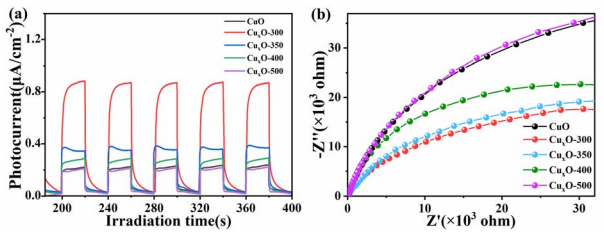

Fig. 7 (a) Transient photocurrent response curve and (b) electrochemical impedance spectroscopy analysis.

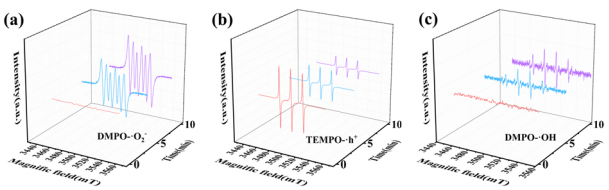

Fig. 8 ESR spectra of Cu$_x$O-300 under different illumination times: (a) $^{\bullet}O_2^-$, (b) h^+, and (c) $^{\bullet}$OH.

Open Access Article. Published on 14 December 2023. Downloaded on 1/19/2026 11:32:41 PM.
This article is licensed under a Creative Commons Attribution-NonCommercial 3.0 Unported Licence.

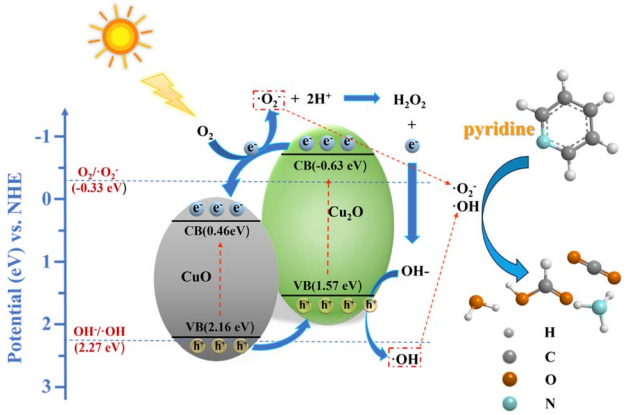

Fig. 9 Possible photocatalytic denitrification mechanism for Cu_xO-300.

active species under visible light irradiation. Based on the above results, the transport of electron–hole pairs in Cu_xO-300 may follow the type II mechanism.

Cu_xO-300 is composed of CuO/Cu_2O nanoparticles, forming a type II semiconductor heterojunction to accelerate the separation of carriers. Based on the above experimental results, a possible fuel denitrification mechanism was proposed (Fig. 9). Under visible light irradiation, both CuO and Cu_2O can generate hole–electron pairs, and the electrons of both migrate from the VB maximum to the CB minimum. At the same time, because the conduction band potential of Cu_2O is more significant (−0.63 eV *vs.* NHE) and the VB maximum is smaller (1.57 eV *vs.* NHE), the electrons of Cu_2O migrate to the CB minimum of CuO through the heterojunction. The holes (h^+) of CuO are beneficial to transfer to the VB maximum of Cu_2O in energy. The e^- can capture the dissolved O_2 accumulated in the CB minimum of CuO to form the main active substance $^{\cdot}O_2^-$ ($e^- + O_2 \rightarrow {}^{\cdot}O_2^-$), which is involved in the photocatalytic degradation of pyridine. At the same time, since the VB maximum of Cu_2O (1.57 eV *vs.* NHE) and CuO (2.16 eV *vs.* NHE) are lower than $E_{(H_2O/OH)}$ (2.27 eV *vs.* NHE), $^{\cdot}OH$ cannot be generated under visible light irradiation, and $^{\cdot}O_2^-$ radicals are required to further react with H^+ and holes to generate $^{\cdot}OH$ radicals. The active substances $^{\cdot}O_2^-$ and $^{\cdot}OH$ are involved in the degradation of pyridine.[54] In fuel denitrification, pyridine is combined with $^{\cdot}O_2^-$ and $^{\cdot}OH$ to form cyclic and ring-opening intermediates, eventually oxidizing into small molecules. On the one hand, the improvement of photocatalytic performance of Cu_xO-300 is attributed to forming a type II semiconductor heterojunction, which constructs a fast electron transport channel and promotes the separation of carriers. On the other hand, the Cu^+/Cu^{2+} metal center formed based on the MOF framework as a Lewis acid site can better adsorb pyridine through coordination and promote photocatalytic reactions.

Conclusions

In summary, the Cu_xO-*T* composite was prepared with HKUST-1(Cu) as the pre-sacrifice, and then the activity of the prepared photocatalyst was investigated. Under visible light (≥420 nm) irradiation, the photocatalytic activity of Cu_xO-300 composites still maintaining the original HKUST-1(Cu) framework was significantly improved (~81%, 4 h). Based on the experimental results, it can be concluded that the significant performance improvement was primarily due to the presence of abundant Lewis acid active sites, which Cu^+/Cu^{2+} formed through Cu_xO-300 in the octahedral structure. Additionally, mixed-valence metal oxide heterojunction formation enhances its visible light absorption performance and facilitates the separation of photogenerated carriers. This study is expected to provide a reference for preparing porous metal oxides at different temperatures and a basis for rapidly adjusting the surface structure of fuel denitrification photocatalysts.

Author contributions

Conceptualization: R. H. and R. L.; investigation: J. L., R. H.; L. C., Y. X. and G. Y.; writing—review and editing: J. L. All authors have read and agreed to the published version of the manuscript.

Conflicts of interest

The authors declare no conflict of interest.

Acknowledgements

This work was financially supported by program for National Natural Science Foundation of China (22372085), Innovative Research Team in Science and Technology in Fujian Province University, Natural Science Foundation of Fujian Province (2023H6023, 2023J011067), Research Project of Ningde Normal University (No. 2023ZX02, 2022FZ18).

References

1 B. N. Bhadra and S. H. Jhung, *Chem. Eng. J.*, 2020, **398**, 125590.
2 X. D. Lang, Q. W. Li, Y. C. Xu, M. M. Ji, G. Yan and S. H. Guo, *Bioresour. Technol.*, 2019, **290**, 121719.
3 L. Wang, D. X. Xie, Y. Y. Ma, M. Sun, N. Mominou, W. J. Jiang, S. F. Chen and C. Y. Jing, *Fuel Process. Technol.*, 2021, **216**, 106802.
4 S. Albersberger, J. Hein, M. W. Schreiber, S. Guerra, J. Y. Han, O. Y. Gutierrez and J. A. Lercher, *Catal. Today*, 2017, **297**, 344–355.
5 R. D. Deese, R. E. Morris, A. E. Metz, K. M. Myers, K. Johnson and T. N. Loegel, *Energy Fuels*, 2019, **33**, 6659–6669.
6 N. E. Paucar, P. Kiggins, B. Blad, K. De Jesus, F. Afrin, S. Pashikanti and K. Sharma, *Environ. Chem. Lett.*, 2021, **19**, 1205–1228.
7 H. Y. Yao, Y. A. Ren, X. Q. Deng and C. H. Wei, *J. Hazard. Mater.*, 2011, **186**, 1136–1140.
8 Y. M. Zhang, L. Chang, N. Yan, Y. X. Tang, R. Liu and B. E. Rittmann, *Environ. Sci. Technol.*, 2014, **48**, 649–655.

© 2023 The Author(s). Published by the Royal Society of Chemistry

Open Access Article. Published on 14 December 2023. Downloaded on 1/19/2026 11:32:41 PM. This article is licensed under a Creative Commons Attribution-NonCommercial 3.0 Unported Licence.

9 H. Y. Yao, G. Wang, C. C. Zuo, C. S. Li, E. Q. Wang and S. J. Zhang, *Green Chem.*, 2017, **19**, 1692–1700.
10 L. P. Zheng, G. Y. Yan, Y. Y. Huang, X. X. Wang, J. L. Long, L. Li and T. Y. Xu, *Int. J. Hydrogen Energy*, 2014, **39**, 13401–13407.
11 S. H. Wang, Z. J. He, L. Wu, D. L. Wang, R. R. Si, X. Y. Liu and R. W. Liang, *Dalton Trans.*, 2023, **52**, 3517–3525.
12 T. Chen, Z. J. Zhu, F. Chen, C. Hu and H. W. Huang, *Appl. Surf. Sci.*, 2023, **616**, 156467.
13 W. N. Hu, M. M. Jiang, R. W. Liang, R. K. Huang, Y. Z. Xia, Z. Y. Liang and G. Y. Yan, *Dalton Trans.*, 2021, **50**, 2596–2605.
14 D. L. Wang, E. R. Zhan, S. H. Wang, X. Y. Liu, G. Y. Yan, L. Chen and X. X. Wang, *Molecules*, 2023, **28**, 282.
15 Y. Lu, H. B. Pan, J. F. Lai, Y. Z. Xia, L. Chen, R. W. Liang, G. Y. Yan and R. K. Huang, *RSC Adv.*, 2022, **12**, 12702–12709.
16 M. A. Badillo-Avila, R. Castanedo-Perez, G. Torres-Delgado, J. Marquez-Marin and O. Zelaya-Angel, *Mater. Sci. Semicond. Process.*, 2018, **74**, 203–209.
17 X. Cheng, Y. Liu, L. Zheng, F. Tan, C. Luo, B. Xu, J. Xu, X. Zhu, D. Wu and H. Liang, *J. Colloid Interface Sci.*, 2022, **626**, 1028–1039.
18 M. Jin, X. Ban, J. Gao, J. Chen, D. K. Hensley, H. C. Ho, R. J. Percoco, C. M. Ritzi and Y. Yue, *Inorg. Chem.*, 2019, **58**, 8332–8338.
19 H. C. Huang, W. G. Zhang, H. X. Wang, A. L. Wei, J. Wang and Y. M. Liu, *Int. J. Hydrogen Energy*, 2023, **48**, 25366–25378.
20 M. Lan, G. L. Fan, L. Yang and F. Li, *RSC Adv.*, 2015, **5**, 5725–5734.
21 H. X. Duo, X. F. Lu, X. B. Nie, L. C. Wang, S. Wang, X. J. Liang and Y. Guo, *J. Chromatogr. A*, 2020, **1626**, 461328.
22 P. Yu, Y. Han, D. Han, X. Liu, Y. Liang, Z. Li, S. Zhu and S. Wu, *J. Hazard. Mater.*, 2020, **390**, 122126.
23 Y. Chen, D. Yang, X. Xin, Z. S. Yang, Y. C. Gao, Y. H. Shi, Z. F. Zhao, K. An, W. J. Wang, J. D. Tan and Z. Y. Jiang, *J. Mater. Chem. A*, 2022, **10**, 9717–9725.
24 L. Zhang and J. Q. Zhang, *Front. Energy*, 2019, **13**, 221–250.
25 J. D. Xiao, L. L. Han, J. Luo, S. H. Yu and H. L. Jiang, *Angew. Chem., Int. Ed.*, 2018, **57**, 1103–1107.
26 R. W. Liang, Z. Y. Liang, F. Chen, D. H. Xie, Y. L. Wu, X. X. Wang, G. Y. Yan and L. Wu, *Chin. J. Catal.*, 2020, **41**, 188–199.
27 W. X. Zhou, Y. J. Tang, X. Y. Zhang, S. T. Zhang, H. G. Xue and H. Pang, *Coord. Chem. Rev.*, 2023, **477**, 214949.
28 P. Behera, A. Ray, S. P. Tripathy, L. Acharya, S. Subudhi and K. Parida, *J. Photochem. Photobiol., A*, 2023, **436**, 114415.
29 A. Ray, S. Subudhi, S. P. Tripathy, L. Acharya and K. Parida, *Adv. Mater. Interfaces*, 2022, **9**, 2201440.
30 D. X. Yan, J. Y. Xin, Q. Zhao, K. Gao, X. M. Lu, G. Y. Wang and S. J. Zhang, *Catal. Sci. Technol.*, 2018, **8**, 164–175.
31 J. Panda, S. P. Tripathy, S. Dash, A. Ray, P. Behera, S. Subudhi and K. Parida, *Nanoscale*, 2023, **15**, 7640–7675.
32 P. Behera, S. Subudhi, S. P. Tripathy and K. Parida, *Coord. Chem. Rev.*, 2022, **456**, 214392.
33 S. Subudhi, G. Swain, S. P. Tripathy and K. Parida, *Inorg. Chem.*, 2020, **59**, 9824–9837.
34 M. Bagheri, A. Melillo, B. Ferrer, M. Y. Masoomi and H. Garcia, *ACS Appl. Mater. Interfaces*, 2022, **14**, 978–989.
35 Y. F. Zhu, Y. F. Liu, Q. Ai, G. H. Gao, L. Yuan, Q. Y. Fang, X. Y. Tian, X. Zhang, E. Egap, P. M. Ajayan and J. Lou, *ACS Mater. Lett.*, 2022, **4**, 464–471.
36 Q. Zheng, J. Wang, X. Li, Y. Bai, Y. P. Li, J. C. Wang, Y. Y. Shi, X. Y. Jiang and Z. Q. Li, *ACS Mater. Lett.*, 2022, **4**, 1638–1645.
37 X. Zhao, Y. Tan, F. Wu, H. Niu, Z. Tang, Y. Cai and J. P. Giesy, *Sci. Total Environ.*, 2016, **571**, 380–387.
38 H. T. Li, L. J. Ban, Z. Z. Niu, X. Huang, P. F. Meng, X. D. Han, Y. Zhang, H. X. Zhang and Y. X. Zhao, *Nanomaterials*, 2019, **9**, 1301.
39 B. Di Credico, M. Redaelli, M. Bellardita, M. Calamante, C. Cepek, E. Cobani, M. D'Arienzo, C. Evangelisti, M. Marelli, M. Moret, L. Palmisano and R. Scotti, *Catalysts*, 2018, **8**, 353.
40 S. Mosleh, M. R. Rahimi, M. Ghaedi, K. Dashtian and S. Hajati, *RSC Adv.*, 2016, **6**, 17204–17214.
41 Y. Wu, Y. Q. Li, H. Li, H. Guo, Q. Yang and X. M. Li, *Sep. Purif. Technol.*, 2022, **303**, 122106.
42 Z. D. Wang, Y. Zang, Z. J. Liu, P. Peng, R. Wang and S. Q. Zang, *Appl. Catal., B*, 2021, **288**, 119941.
43 C. Prestipino, L. Regli, J. G. Vitillo, F. Bonino, A. Damin, C. Lamberti, A. Zecchina, P. L. Solari, K. O. Kongshaug and S. Bordiga, *Chem. Mater.*, 2006, **18**, 1337–1346.
44 Y. Xiong, L. Che, Z. Fu and P. Ma, *Adv. Powder Technol.*, 2018, **29**, 1331–1338.
45 Y. Y. Song, B. Dong, S. W. Wang, Z. R. Wang, M. J. Zhang, P. Tian, G. C. Wang and Z. Zhao, *ACS Omega*, 2020, **5**, 6260–6269.
46 C. K. Tsai, C. H. Huang, J. J. Horng, H. L. Ong and R. A. Doong, *Nanomaterials*, 2023, **13**, 282.
47 Q. Meng, W. Liu, J. Jiang and X. Zhang, *Ceram. Int.*, 2021, **47**, 19402–19413.
48 Y. Zhu, D. Y. Li, S. Y. Zuo, Z. Y. Guan, S. Ding, D. S. Xia and X. H. Li, *J. Environ. Chem. Eng.*, 2021, **9**, 106781.
49 N. H. Khdary, W. S. Alkhuraiji, T. S. Sakthivel, D. N. Khdary, M. A. Salam, S. Alshihri, S. I. Al-Mayman and S. Seal, *Catalysts*, 2020, **10**, 872.
50 S. P. Tripathy, S. Subudhi, A. Ray, P. Behera, A. Bhaumik and K. Parida, *Langmuir*, 2022, **38**, 1766–1780.
51 S. Subudhi, S. P. Tripathy and K. Parida, *Inorg. Chem. Front.*, 2021, **8**, 1619–1636.
52 D. Tahir and S. Tougaard, *J. Phys.: Condens. Matter*, 2012, **24**, 175002.
53 S. Mosleh, M. R. Rahimi, M. Ghaedi, K. Dashtian and S. Hajati, *Ultrason. Sonochem.*, 2018, **40**, 601–610.
54 R. Liang, S. Wang, Y. Lu, G. Yan, Z. He, Y. Xia, Z. Liang and L. Wu, *Molecules*, 2021, **26**, 7566.

© 2023 The Author(s). Published by the Royal Society of Chemistry